


**Magnon blockade induced by parametric amplification**Wei Zhang,<sup>1</sup> Shutian Liu,<sup>1,\*</sup> Shou Zhang,<sup>2,†</sup> and Hong-Fu Wang<sup>2,‡</sup><sup>1</sup>*School of Physics, Harbin Institute of Technology, Harbin, Heilongjiang 150001, China*<sup>2</sup>*Department of Physics, College of Science, Yanbian University, Yanji, Jilin 133002, China* (Received 4 December 2023; revised 12 February 2024; accepted 8 April 2024; published 19 April 2024)

We propose to achieve and enhance the magnon blockade effect in an optomechanical-magnetic system based on a quantum destructive interference mechanism between three indirect transition pathways. By introducing a degenerate parametric amplifier, we analytically obtain the optimal parametric gain and phase for achieving the magnon blockade. Under the optimized parameter conditions, the driving detunings of cavity and magnon modes can be flexibly controlled to achieve the smallest second-order magnon correlation function. Moreover, the magnon blockade can exhibit fascinating features by proper driving detuning and weaker driving strength. Our scheme combines the benefits of destructive interference-induced magnon blockade and energy-level anharmonicity-induced magnon blockade, which results in a reduction of equal-time second-order magnon correlation while simultaneously avoiding time-delay second-order magnon correlation with rapid oscillation. Our work provides an alternative and experimentally feasible platform for manipulating few-magnon states and generating single-magnon sources.

DOI: [10.1103/PhysRevA.109.043712](https://doi.org/10.1103/PhysRevA.109.043712)**I. INTRODUCTION**

Hybrid quantum systems involving microwave cavity photons and magnons characterized by collective spin excitations in yttrium iron garnet (YIG) have aroused extensive attention with regard to the implementation of quantum cryptography [1,2] and quantum information processing [3,4]. It has been experimentally demonstrated that the strong or ultrastrong coupling between magnons of YIG and cavity photons can be created through a magnetic dipole interaction [5–8], which arises from the fact that the YIG possesses an extremely high spin density and a low damping rate [9,10]. Based on such hybrid systems, many fascinating phenomena such as the ground-state cooling of a magnomechanical resonator [11–13], bipartite or tripartite entanglement [14,15], magnon quadrature squeezing [16,17], and magnon blockade (MB) [18–23] have been verified in theory and experiment.

Recently, as a typical pure quantum effect, the investigation of the magnon blockade has drawn considerable concern and made substantial progress. Analogous to the photon blockade (PB) [24–27], the MB can be generated through two physical mechanisms. One depends on the system energy-level anharmonicity [18,20,22,23,28–31] where the second magnon will be prohibited when the first magnon is excited to the single-magnon state, known as conventional magnon blockade (CMB). The other mechanism relies on the destructive interference [26,32–38] between different transition pathways from a one-magnon state to a two-magnon state, called unconventional magnon blockade (UMB). Compared to the CMB,

the UMB is possible in a weak-coupling scenario, which is not a challenging task in the magnetic domain and is experimentally much easier to achieve. The MB was first theoretically implemented in a hybrid ferromagnet-superconductor hybrid system by appropriately selecting qubit-magnon strength and driving detuning [18]. Subsequently, many schemes have been proposed to obtain the antibunched light based on the MB effect, such as CMB in an optomechanical-magnetic system assisted by a two-level atom [22], quantum-interference-enhanced MB in an YIG coupled to superconducting circuits [20,39], tunable MB in a ferromagnet-superconductor system with two qubits [40], phase-controlled MB in a cavity magnetic system with a three-level atom [41], and parity-time symmetry-enhanced MB in a cavity magnon system [42].

On the other hand, directional parametric amplification has been employed in microring resonator systems to achieve a nonreciprocal photon blockade effect without the need for Sagnac-Fizeau shifts produced by rotating the resonator [43–47]. This could be interpreted to mean that parametric amplification promotes the enhancement of the nonlinear coupling strength [48–51]. In addition, it has been utilized to realize frequency conversion [52,53] and to obtain photon sources [54]. In particular, the authors in Ref. [55] constructed an all-optical diode and three-port quasicirculator by nonreciprocity induced by the parametric amplification. Moreover, Wei *et al.* have successfully enhanced the phonon blockade effect by applying a degenerate parametric drive to the mechanical oscillator [56]. The aforementioned studies sufficiently illustrate the significance of the parametric amplification in generating the blockade effect. However, here we utilize the parametric amplification to generate a magnon blockade.

In this paper, we consider a hybrid optomechanical-magnetic system aiming to study the generation of the MB.

\*stliu@hit.edu.cn

†szhang@ybu.edu.cn

‡hfwang@ybu.edu.cn

A degenerate optical parametric amplifier (OPA) is placed in the optomechanical cavity [57,58], which has enabled many interesting phenomena such as the generation of squeezed light [48], the improvement of mechanical ground-state cooling [59,60], and the enhancement of precise measurement [61]. Here we utilize the parametric amplification induced by the OPA to increase a new transition pathway, resulting in an enhanced destructive interference. To begin with, we prove the rationality of approximation from the original Hamiltonian to the effective Hamiltonian, whereby a three-mode system is simplified as a two-mode system consisting of magnon and photon modes. Then we analytically derive the optimal conditions for strong magnon antibunching and find that the analytical solutions agree well with the numerical simulations. Based on the optimal conditions, we show that the MB is strongly dependent on the parametric gain and driving phase. Moreover, the driving detunings of the cavity and magnon modes for the smallest second-order magnon correlation function can be flexibly tuned. Interestingly, by selecting specific driving detunings of the cavity and magnon, along with optimal parametric gain and phase, our scheme can combine the advantages of the UMB and the CMB, which reduces  $g_m^{(2)}(0)$  and simultaneously avoids  $g_m^{(2)}(\tau)$  with rapid oscillation. Finally, we discuss the thermal magnon and photon excitations on the MB and find that the thermal bath for photon and magnon modes has a negligible impact on the results. Our work opens up a different route to implement the quantum manipulation of a single-magnon level and prepare magnon sources, which may have a significant practical relevance for precision metrology and quantum information processing.

The paper is organized as follows: In Sec. II, we introduce the hybrid optomechanical-magnetic system with an OPA, describe the system dynamics using a general master equation, and verify the rationality of the Hamiltonian approximation. In Sec. III, we analytically obtain the optimized parameter conditions for the MB, further combine the advantages of the UMB and the CMB by choosing proper driving detunings of cavity and magnon modes, and investigate the influence of thermal photon and magnon excitations on the MB effect. Finally, we present the conclusion in Sec. IV.

## II. SYSTEM MODEL AND THEORETICAL FRAMEWORK

As schematically shown in Fig. 1, we consider a hybrid optomechanical-magnetic system consisting of a small YIG sphere and an OPA. The system contains a cavity mode with resonance frequency  $\omega_c$ , a magnon mode with resonance frequency  $\omega_m$ , and a phonon mode with resonance frequency  $\omega_b$ . The cavity mode couples with the magnon and phonon modes via magnetic dipole and radiation pressure, respectively. The cavity mode interacts with the OPA pumped by an external laser with frequency  $\omega_d$ . In order to achieve an antibunching effect, it is necessary to coherently drive the cavity mode using an external weak field with frequency  $\omega_l$ . The Hamiltonian of the three-mode system can be written as ( $\hbar = 1$ )

$$\begin{aligned}
 H = & \omega_c a^\dagger a + \omega_b b^\dagger b + \omega_m m^\dagger m + g a^\dagger a (b^\dagger + b) \\
 & + G_m (a^\dagger m + a m^\dagger) + E (a^\dagger e^{-i\omega_l t} + a e^{i\omega_l t}) \\
 & + G (e^{i\theta} a^{\dagger 2} e^{-i\omega_d t} + e^{-i\theta} a^2 e^{i\omega_d t}), \quad (1)
 \end{aligned}$$

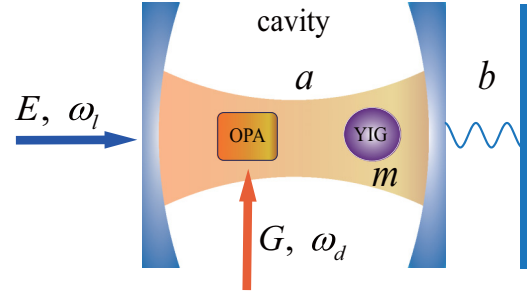


FIG. 1. Sketch of the hybrid quantum system. A degenerate parametric amplifier is placed in an optomechanical cavity coupled to a small YIG sphere. The cavity mode  $a$  is pumped by an external weak field with amplitude  $E$  and frequency  $\omega_l$ . The parametric amplification with amplitude  $G$  and frequency  $\omega_d$  on the cavity is generated by pumping the parametric amplifier. The cavity mode  $a$  couples to the magnon mode  $m$  and phonon mode  $b$  through magnetic dipole interaction and radiation-pressure interaction, respectively.

where  $a$  ( $a^\dagger$ ),  $m$  ( $m^\dagger$ ), and  $b$  ( $b^\dagger$ ) represent the annihilation (creation) operators of the cavity, magnon, and phonon, respectively. The first three terms are the free energies of the cavity, magnon, and phonon modes, respectively. The fourth term describes the optomechanical interaction with single-photon coupling strength  $g$ , and the fifth term describes the magnetic dipole interaction between the cavity and magnon modes with coupling strength  $G_m$ . The last term represents the coupling between the cavity field and the OPA with the parametric gain  $G$ , depending on the power of the pump driving the OPA, and the phase of the pump driving the OPA  $\theta$ . It is worthy mentioning that in a recent experiment, the authors utilized backward Raman amplification to enhance the phase-insensitive parametric gain, which in turn improves the phase-sensitive operation [62]. Moreover, with current laser technologies, the parametric pump has the stable frequency and phase during a timescale of  $\mu\text{s}$  [63,64]. In the rotating frame with respect to  $\omega_l(a^\dagger a + m^\dagger m)$ , and adopting  $\omega_d = 2\omega_l$ , the Hamiltonian in Eq. (1) can be transformed into a time-independent form,

$$\begin{aligned}
 H_2 = & \Delta_c a^\dagger a + \omega_b b^\dagger b + \Delta_m m^\dagger m + g a^\dagger a (b^\dagger + b) \\
 & + G_m (a^\dagger m + a m^\dagger) + (E a^\dagger + G e^{i\theta} a^{\dagger 2} + \text{H.c.}), \quad (2)
 \end{aligned}$$

where  $\Delta_{c(m)} = \omega_{c(m)} - \omega_l$  is the frequency detuning between the cavity (magnon) mode and the cavity driving field. To show that the Hamiltonian exhibits an anharmonic energy level, we apply a unitary transformation  $U = \exp[g/\omega_b a^\dagger a (b^\dagger - b)]$  to  $H_2$ , leading to a Hamiltonian  $H_3 = U^\dagger H_2 U$  with the form

$$\begin{aligned}
 H_3 = & \Delta_c a^\dagger a + \omega_b b^\dagger b + \Delta_m m^\dagger m - g^2/\omega_b (a^\dagger a)^2 \\
 & + G_m \left[ m a^\dagger e^{-\frac{g}{\omega_b} (b^\dagger - b)} + m^\dagger a e^{\frac{g}{\omega_b} (b^\dagger - b)} \right] \\
 & + E a^\dagger e^{-\frac{g}{\omega_b} (b^\dagger - b)} + G e^{i\theta} a^{\dagger 2} e^{-\frac{2g}{\omega_b} (b^\dagger - b)} + \text{H.c.}, \quad (3)
 \end{aligned}$$

where  $\Delta_g = g^2/\omega_b$ . With the condition  $g \ll \omega_b$ , exponential factors with  $g/\omega_b$  in Hamiltonian (3) can be safely ignored, in

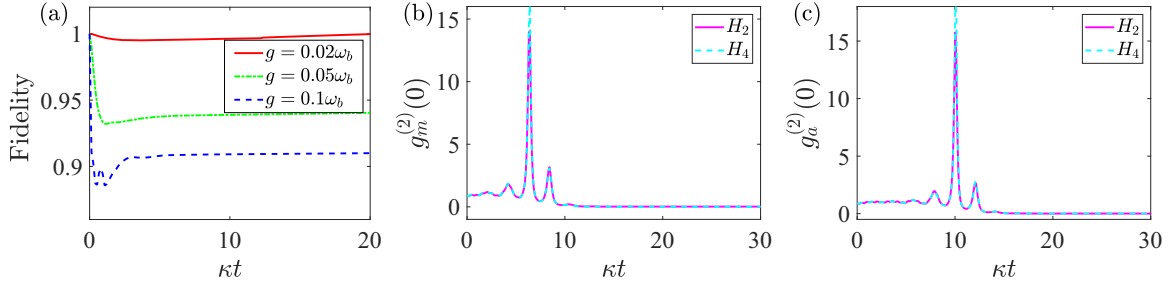


FIG. 2. (a) Time evolution of fidelity  $\mathcal{F}$  for different optomechanical coupling strength  $g$ . (b) Second-order magnon correlation function  $g_m^{(2)}(0)$  and (c) photon correlation function  $g_a^{(2)}(0)$  as a function of  $\kappa t$  with Hamiltonian  $H_2$  (pink line) and  $H_4$  (cyan line). In (b),  $G$  and  $\theta$  are taken as  $G^{\text{opt}} = |E^2(\tilde{\Delta}_a - 2\Delta_g + \tilde{\Delta}_m)/[\tilde{\Delta}_m(\tilde{\Delta}_a - \Delta_g) - G_m^2]|$  and  $\theta = \text{Arg}\{E^2(\tilde{\Delta}_a - 2\Delta_g + \tilde{\Delta}_m)/[\tilde{\Delta}_m(\tilde{\Delta}_a - \Delta_g) - G_m^2]\}$  according to Eq. (13), respectively. In (c),  $G$  and  $\theta$  are taken as  $G_2^{\text{opt}} = |E^2\tilde{\Delta}_m^2(\tilde{\Delta}_a - \Delta_g + \tilde{\Delta}_m)/[G_m^2 - \tilde{\Delta}_m(\tilde{\Delta}_a - \Delta_g)]Z|$  and  $\theta = \text{Arg}\{E^2\tilde{\Delta}_m^2(\tilde{\Delta}_a - \Delta_g + \tilde{\Delta}_m)/[G_m^2 - \tilde{\Delta}_m(\tilde{\Delta}_a - \Delta_g)]Z\}$  according to Eq. (14), respectively. The other parameters are  $\omega_b = 100\kappa$ ,  $\gamma_b = 10^{-6}\omega_b$ ,  $G_m = 3\kappa$ ,  $E = 0.1\kappa$ , and  $\Delta_c = \Delta_m = 0$ .

which case the above Hamiltonian can be rewritten as

$$H_4 = \Delta_c a^\dagger a + \Delta_m m^\dagger m - \Delta_g (a^\dagger a)^2 + G_m (a^\dagger m + am^\dagger) + (Ea^\dagger + Ge^{i\theta}a^{\dagger 2} + \text{H.c.}). \quad (4)$$

It can be known from Eq. (4) that the original optomechanical interaction has changed to a Kerr nonlinearity of the cavity field with strength  $\Delta_g$ . Note that the mechanical oscillator decouples with the cavity field at the same time. Hence, when we are only interested in optical and magnetic properties, we can omit the mechanical part. Next we will demonstrate that the magnon-photon beam-splitter interaction plays a key role in generating the MB. Via considering the dissipation terms of the cavity and magnon modes, the dynamics of the hybrid quantum system can be described by the following master equation:

$$\dot{\rho} = -i[H_4, \rho] + \kappa_a \mathcal{L}[a]\rho + \kappa_m \mathcal{L}[m]\rho, \quad (5)$$

where  $\rho$  is the system density operator, and  $\mathcal{L}[o]\rho = o\rho o^\dagger - (o^\dagger o\rho + \rho o^\dagger o)/2$  ( $o = a, m$ ) is the Lindblad superoperator for operator  $o$ .  $\kappa_a$  ( $\kappa_m$ ) is the decay rate of the cavity (magnon) mode. For the sake of simplicity, it is taken to  $\kappa_a = \kappa_m$  hereafter. The photon and magnon blockade effects can be characterized by the equal-time second-order correlation function,

$$g_a^{(2)}(0) = \frac{\langle a^{\dagger 2} a^2 \rangle}{\langle a^\dagger a \rangle^2} = \frac{\text{Tr}(\rho_{ss} a^{\dagger 2} a^2)}{[\text{Tr}(\rho_{ss} a^\dagger a)]^2},$$

$$g_m^{(2)}(0) = \frac{\langle m^{\dagger 2} m^2 \rangle}{\langle m^\dagger m \rangle^2} = \frac{\text{Tr}(\rho_{ss} m^{\dagger 2} m^2)}{[\text{Tr}(\rho_{ss} m^\dagger m)]^2}, \quad (6)$$

where  $\rho_{ss}$  is the steady-state solution of master equation (5) by setting  $\dot{\rho} = 0$ , and  $g_o^{(2)}(0) = \langle o^{\dagger 2} o^2 \rangle / \langle o^\dagger o \rangle^2$  can be obtained by numerically solving the master equation (5) using the PYTHON package QUTIP [65]. Typically,  $g_o^{(2)}(0) < 1$  implies the sub-Poissonian statistics, corresponding to the photon and magnon antibunching effect. By contrast,  $g_o^{(2)}(0) > 1$  describes the super-Poissonian statistics, corresponding to the bunching effect, meaning that the excitation of the first magnon (photon) favors subsequent magnons (photons). To obtain a nearly perfect magnon (photon) blockade effect, the equal-time second-order correlation function  $g_o^{(2)}(0)$  should tend to zero.

Before giving the analytical results and studying the magnon blockade effect, we first examine the rationality from Hamiltonian (2) to Hamiltonian (4). In Fig. 2(a), we present fidelity  $\mathcal{F}(\rho_1, \rho_2)$  between states  $\rho_1$  governed by  $U^\dagger H_2 U$  and  $\rho_2$  determined by  $H_4$  as a function of time under different coupling strength  $g$ . We can observe that  $\mathcal{F}(\rho_1, \rho_2)$  decreases as optomechanical coupling  $g$  increases, which is consistent with the requirement of the Hamiltonian derivation as illustrated above. For  $g = 0.02\omega_b$ , the value of  $\mathcal{F}(\rho_1, \rho_2)$  in the steady state maintains above 0.999, which is sufficient to guarantee the validity of the approximation. By utilizing  $g = 0.02\omega_b$ , we plot  $g_m^{(2)}(0)$  and  $g_a^{(2)}(0)$  as a function of  $\kappa t$  in Figs. 2(b) and 2(c), respectively. The results show the evolution of  $g^{(2)}(0)$  depending on  $H_2$  and  $H_4$  agrees well, which further proves that the approximation for the Hamiltonian derivation is reasonable.

### III. MAGNON BLOCKADE AND OPTIMAL CONDITIONS

In this part, we are mainly interested in the magnon blockade when the cavity is weakly driven. Before giving a full discussion of the magnon blockade effect, we first prefer to derive the analytical solutions by solving the Schrödinger equation  $i\partial_t|\psi\rangle/\partial t = H_{\text{non}}|\psi\rangle$ , where

$$H_{\text{non}} = H_4 - i\frac{\kappa_a}{2}a^\dagger a - i\frac{\kappa_m}{2}m^\dagger m, \quad (7)$$

and  $|\psi\rangle$  is the wave function of the system, which can be truncated to two excitation subspaces in the weak driving field limit ( $E, G \ll \kappa_a, \kappa_m$ ), and can be written as

$$|\psi\rangle = C_{00}|00\rangle + C_{01}|01\rangle + C_{10}|10\rangle + C_{02}|02\rangle + C_{11}|11\rangle + C_{20}|20\rangle, \quad (8)$$

where  $|C_{am}|^2$  represents the probability of staying in state  $|am\rangle$ .  $|am\rangle = |a\rangle \otimes |m\rangle$  is a direct product state, which means that there are  $a$  photons in the cavity mode and  $m$  magnons in the magnon mode. Substituting the above wave function and non-Hermitian Hamiltonian into the Schrödinger equation, the dynamical equations of the occupying probabilities can be obtained as

$$i\dot{C}_{01} = \tilde{\Delta}_m C_{01} + G_m C_{10} + EC_{11},$$

$$i\dot{C}_{10} = (\tilde{\Delta}_a - \Delta_g)C_{10} + G_m C_{01} + \sqrt{2}EC_{20} + EC_{00},$$

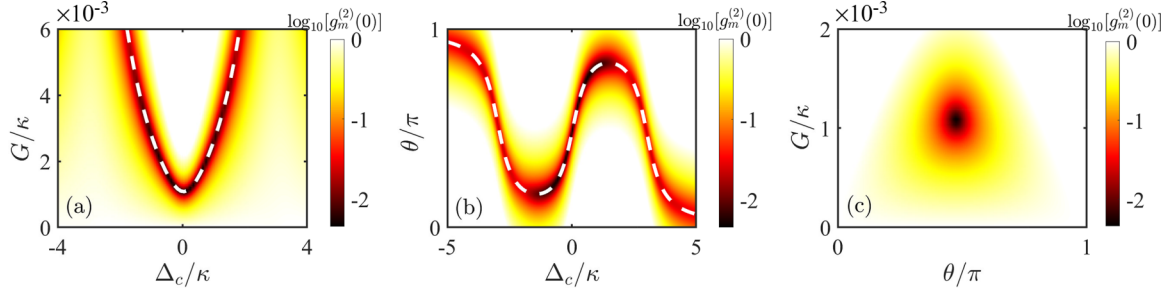


FIG. 3. Second-order magnon correlation function on a logarithmic scale  $\log_{10}[g_m^{(2)}(0)]$  as a function of (a)  $G$ , (b)  $(\theta)$  and the driving detuning  $\Delta_c$ , and (c)  $G$  and  $\theta$ . The white dashed lines represent the optimal conditions decided by Eq. (13).  $\Delta_c = \Delta_m = 0$  is taken in (c). The other parameters are the same as given in Fig. 2.

$$\begin{aligned}
 i\dot{C}_{11} &= (\tilde{\Delta}_m + \tilde{\Delta}_a - \Delta_g)C_{11} + EC_{01} + \sqrt{2}G_m(C_{02} + C_{20}), \\
 i\dot{C}_{02} &= 2\tilde{\Delta}_m C_{02} + \sqrt{2}G_m C_{11}, \\
 i\dot{C}_{20} &= 2(\tilde{\Delta}_a - 2\Delta_g)C_{20} + \sqrt{2}EC_{10} + \sqrt{2}G_m C_{11} \\
 &\quad + \sqrt{2}Ge^{i\theta}C_{00}. \tag{9}
 \end{aligned}$$

With the condition  $C_{00} \simeq 1 \gg C_{01}, C_{10} \gg C_{11}, C_{02}, C_{20}$ , and neglecting the terms of  $C_{11}$  and  $C_{20}$  in the first two in the above equation, the single excitation and two excitation coefficients in the steady state can be solved as

$$\begin{aligned}
 C_{01} &= \frac{-EG_m}{G_m^2 - \tilde{\Delta}_m(\tilde{\Delta}_a - \Delta_g)}, \\
 C_{10} &= \frac{E\tilde{\Delta}_m}{G_m^2 - \tilde{\Delta}_m(\tilde{\Delta}_a - \Delta_g)}, \\
 C_{11} &= \frac{G_m\tilde{\Delta}_m\{E^2(\tilde{\Delta}_a - 2\Delta_g + \tilde{\Delta}_m) + e^{i\theta}G[G_m^2 - \tilde{\Delta}_m(\tilde{\Delta}_a - \Delta_g)]\}}{\Xi}, \\
 C_{02} &= \frac{G_m^2\{E^2(\tilde{\Delta}_a - 2\Delta_g + \tilde{\Delta}_m) + e^{i\theta}G[G_m^2 - \tilde{\Delta}_m(\tilde{\Delta}_a - \Delta_g)]\}}{\sqrt{2}\Xi}, \\
 C_{20} &= \frac{\tilde{\Delta}_m E^2(\tilde{\Delta}_a - \Delta_g + \tilde{\Delta}_m) - e^{i\theta}G[G_m^2 - \tilde{\Delta}_m(\tilde{\Delta}_a - \Delta_g)]Z}{\sqrt{2}\Xi}, \tag{10}
 \end{aligned}$$

where  $\tilde{\Delta}_{m(a)} = \Delta_{m(a)} - i\kappa/2$ ,  $Z = G_m^2 - \tilde{\Delta}_m(\tilde{\Delta}_a - \Delta_g + \tilde{\Delta}_m)$ , and

$$\begin{aligned}
 \Xi &= [G_m^2 - \tilde{\Delta}_m(\tilde{\Delta}_a - \Delta_g)][G_m^2(\tilde{\Delta}_a - 2\Delta_g + \tilde{\Delta}_m) \\
 &\quad - \tilde{\Delta}_m(\tilde{\Delta}_a - 2\Delta_g)(\tilde{\Delta}_a - \Delta_g + \tilde{\Delta}_m)]. \tag{11}
 \end{aligned}$$

Then the equal-time second-order magnon and photon correlation functions can be expressed as

$$\begin{aligned}
 g_m^{(2)}(0) &= \frac{2|C_{02}|^2}{(|C_{01}|^2 + 2|C_{02}|^2 + |C_{11}|^2)^2} \approx \frac{2|C_{02}|^2}{|C_{01}|^4}, \\
 g_a^{(2)}(0) &= \frac{2|C_{20}|^2}{(|C_{10}|^2 + 2|C_{20}|^2 + |C_{11}|^2)^2} \approx \frac{2|C_{20}|^2}{|C_{10}|^4}. \tag{12}
 \end{aligned}$$

Then, the realization of  $g_m^{(2)}(0) \rightarrow 0$  and  $g_a^{(2)}(0) \rightarrow 0$  requires  $C_{02} = 0$  and  $C_{20} = 0$ , respectively, which indicates the nearly perfect MB and PB. Hence, one can obtain the condition of the destructive interference-induced MB as

$$G^{\text{opt}} e^{i\theta} = \frac{E^2(\tilde{\Delta}_a - 2\Delta_g + \tilde{\Delta}_m)}{\tilde{\Delta}_m(\tilde{\Delta}_a - \Delta_g) - G_m^2}. \tag{13}$$

Similarly, the condition of the destructive interference-induced PB can be obtained as

$$G_2^{\text{opt}} e^{i\theta} = \frac{E^2\tilde{\Delta}_m^2(\tilde{\Delta}_a - \Delta_g + \tilde{\Delta}_m)}{[G_m^2 - \tilde{\Delta}_m(\tilde{\Delta}_a - \Delta_g)]Z}. \tag{14}$$

To verify the optimal UMB condition, we plot the equal-time second-order magnon correlation function on a logarithmic scale  $\log_{10}[g_m^{(2)}(0)]$  as a function of  $\Delta_c$  and  $G$  ( $\theta$ ) in Figs. 3(a) and 3(b), where the white dashed lines present the optimal values to realize the UMB. It is obvious that as the driving detuning increases,  $G$  is required to increase to balance the influence on the optimal conditions. Furthermore, the plot of  $\log_{10}[g_m^{(2)}(0)]$  as a function of  $\theta$  and  $G$  is shown in Fig. 3(c) with  $\Delta_c = \Delta_m = 0$ . It is found that when  $\theta = 0.4755\pi$  and  $G = 0.0011\kappa$ , there exists a minimum value of  $\log_{10}[g_m^{(2)}(0)]$ , which is consistent with the optimal UMB condition. In the following study, we adopt the optimal parameters  $G$  and  $\theta$  to explore the MB effect.

Figures 4(a) and 4(b) show the equal-time second-order correlation function on a logarithmic scale  $\log_{10}[g^{(2)}(0)]$  as a function of the detuning  $\Delta_c$  under the optimal condition of UMB and UPB, respectively. When the selected parameters

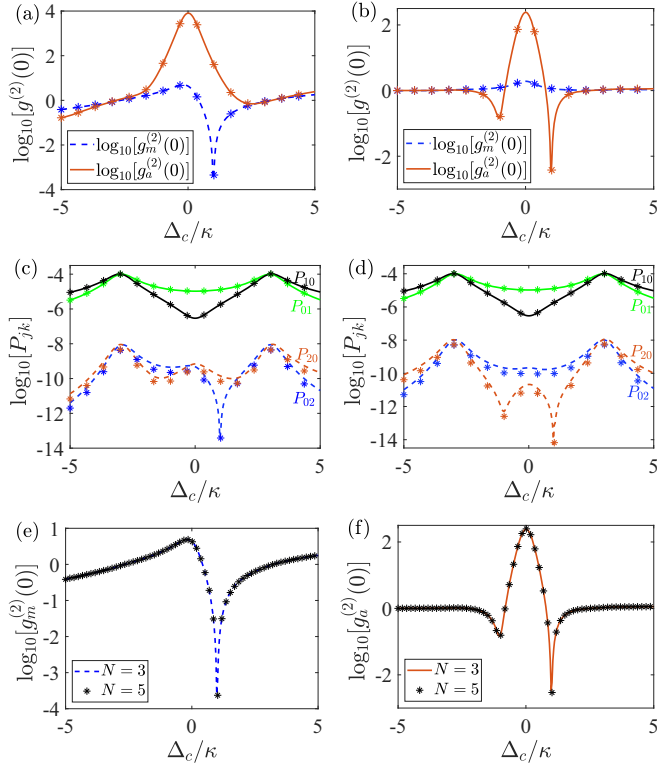


FIG. 4. (a), (b) Second-order magnon and photon correlation functions on a logarithmic scale  $\log_{10}[g_m^{(2)}(0)]$  and  $\log_{10}[g_a^{(2)}(0)]$  as a function of the driving detuning  $\Delta_c$ . (c), (d) Photon-number and magnon-number distributions  $P_{n,m=1,2}$  as a function of the driving detuning  $\Delta_c$ . The solid and dashed lines are the exact numerical results obtained by solving Eqs. (5) and (6), and asterisks indicate the analytical solutions given by Eq. (12). (e)  $\log_{10}[g_m^{(2)}(0)]$  and (f)  $\log_{10}[g_a^{(2)}(0)]$  as a function of the driving detuning  $\Delta_c$ , where blue and orange lines and black asterisks indicate that the number of Fock states is truncated to  $N = 3$  and  $N = 5$  for the two modes, respectively.  $E = 0.01\kappa$  is taken in all the plots. The other parameters are the same as given in Fig. 2.

satisfy the conditions of destructive interference-induced MB or PB, optimal detuning points for realizing the MB and the PB correspond to photon bunching and magnon bunching, respectively. One can find that  $\Delta_c = \kappa$  is the optimal UMB and UPB condition, in conjunction with other parameters ensuring the optimal parametric gain  $G$  and phase  $\theta$ . Moreover, the results from Figs. 4(a) and 4(b) demonstrate that parameter conditions for achieving the MB and PB are entirely different. Furthermore, we also present photon-number and magnon-number distributions  $P_{n,m=1,2}$  defined by  $P_{n(m)} = \text{Tr}[|n(m)\rangle_{oo}\langle n(m)|\rho_{ss}]$  as a function of the driving detuning  $\Delta_c$  in Figs. 4(c) and 4(d), respectively, corresponding to the optimal conditions decided by Eqs. (13) and (14). Because of that, the blockades depend on the destructive interference mechanism rather than the energy-level anharmonicity; the detunings corresponding to the smallest  $\log_{10}[g_o^{(2)}(0)]$  are not the detunings contributing to the largest mean magnon or photon numbers. In contrast, the dips in distributions  $P_{02}$  and  $P_{20}$  demonstrate the result of the quantum destructive interference. In the numerical simulation in the above figures, the Fock spaces of the magnon and photon

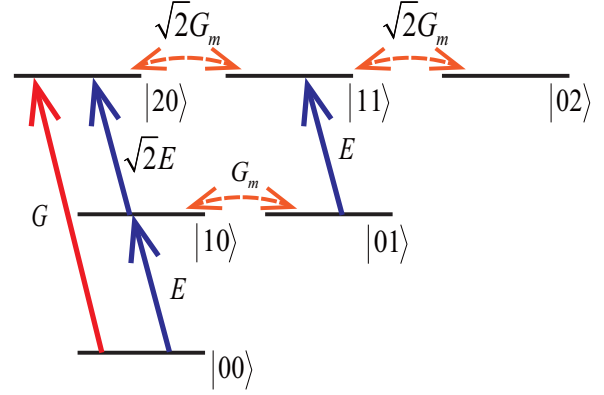


FIG. 5. Energy-level diagram of the system showing the zero-, one-, and two-magnon states (horizontal black lines without arrows) and the corresponding transition pathways (color lines with arrows) leading to the destructive interference for preventing the two-magnon occupation.

modes are truncated to  $N = 3$ , which allows for up to two magnons or photons to be excited. To verify the validity of the numerical results, we plot  $\log_{10}[g_m^{(2)}(0)]$  and  $\log_{10}[g_a^{(2)}(0)]$  for different numbers of Fock states in Figs. 4(e) and 4(f), respectively. It can be seen that there is almost no difference in the steady-state correlation functions. In other words, the determination of the steady-state regime is not significantly affected even as the number of truncated Fock states continues to increase under the current parameters.

Next, we will proceed to investigate physical causes of the MB and the PB. As shown in Fig. 5, for the UPB, there are three excitation pathways to reach the two-photon state: two direct excitations (a)  $|00\rangle \xrightarrow{G} |20\rangle$ , (b)  $|00\rangle \xrightarrow{E} |10\rangle \xrightarrow{\sqrt{2}E} |20\rangle$ , and one indirect excitation (c)  $|00\rangle \xrightarrow{E} |10\rangle \xrightarrow{G_m} |01\rangle \xrightarrow{E} |11\rangle \xrightarrow{\sqrt{2}G_m} |20\rangle$ . When the optimal conditions are satisfied, the two-photon state cannot be occupied due to the quantum destructive interference between three excitation pathways. Meanwhile, there are three excitation pathways to reach the two-magnon state which is different with three indirect pathways: (a)  $|00\rangle \xrightarrow{G} |20\rangle \xrightarrow{\sqrt{2}G_m} |11\rangle \xrightarrow{\sqrt{2}G_m} |02\rangle$ , (b)  $|00\rangle \xrightarrow{E} |10\rangle \xrightarrow{\sqrt{2}E} |20\rangle \xrightarrow{\sqrt{2}G_m} |11\rangle \xrightarrow{\sqrt{2}G_m} |02\rangle$ , and (c)  $|00\rangle \xrightarrow{E} |10\rangle \xrightarrow{G_m} |01\rangle \xrightarrow{E} |11\rangle \xrightarrow{\sqrt{2}G_m} |02\rangle$ . Different transition pathways naturally lead to different optimal parametric gain  $G$  and phase  $\theta$  for achieving UPB and UMB.

The cavity-magnon coupling  $G_m$  occurs multiple times in the transition pathways to access the two-magnon state, which could play an essential role in the generation of the MB. We plot  $\log_{10}[g_m^{(2)}(0)]$  and  $\log_{10}[g_a^{(2)}(0)]$  as a function of  $G_m/\kappa$  in Fig. 6(a). The optimal parameter conditions including parametric gain  $G$  and phase  $\theta$  for individual blockades are taken. Under these parameter conditions,  $\log_{10}[g_m^{(2)}(0)]$  decreases as cavity-magnon coupling strength  $G_m$  increases ( $G_m = 0$  leads to no MB, not shown here), which is completely in line with our conjecture. This can be interpreted to mean that  $G_m$  participates in each pathway to attain the two-magnon state, that is to say, interference pathways would not form in the absence of  $G_m$ . In contrast,  $\log_{10}[g_a^{(2)}(0)]$  increases as cavity-magnon coupling strength  $G_m$  increases. The role of

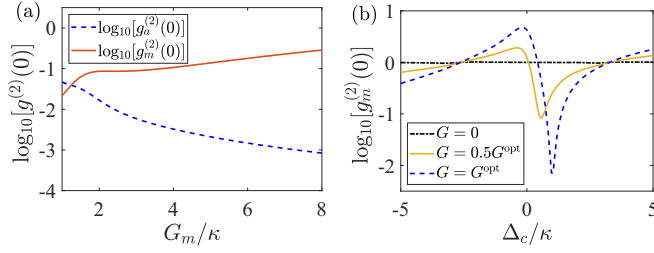


FIG. 6. (a) Second-order magnon and photon correlation functions on a logarithmic scale  $\log_{10}[g_a^{(2)}(0)]$  and  $\log_{10}[g_m^{(2)}(0)]$  as a function of cavity-magnon coupling strength  $G_m$ . (b) Second-order magnon correlation function on a logarithmic scale  $\log_{10}[g_m^{(2)}(0)]$  as a function of  $\Delta_c$  for different parametric amplification  $G$ .  $\Delta_c = \Delta_m = \kappa$  is used in (a), and  $\Delta_c = \Delta_m$  in (b). In (a), for magnon blockade,  $G$  and  $\theta$  are taken as  $G^{\text{opt}} = |E^2(\tilde{\Delta}_a - 2\tilde{\Delta}_g + \tilde{\Delta}_m)/[\tilde{\Delta}_m(\tilde{\Delta}_a - \tilde{\Delta}_g) - G_m^2]|$  and  $\theta = \text{Arg}\{E^2(\tilde{\Delta}_a - 2\tilde{\Delta}_g + \tilde{\Delta}_m)/[\tilde{\Delta}_m(\tilde{\Delta}_a - \tilde{\Delta}_g) - G_m^2]\}$  according to Eq. (13), respectively, and for photon blockade,  $G$  and  $\theta$  are taken as  $G_2^{\text{opt}} = |E^2\tilde{\Delta}_m^2(\tilde{\Delta}_a - \tilde{\Delta}_g + \tilde{\Delta}_m)/[G_m^2 - \tilde{\Delta}_m(\tilde{\Delta}_a - \tilde{\Delta}_g)Z]|$  and  $\theta = \text{Arg}\{E^2\tilde{\Delta}_m^2(\tilde{\Delta}_a - \tilde{\Delta}_g + \tilde{\Delta}_m)/[G_m^2 - \tilde{\Delta}_m(\tilde{\Delta}_a - \tilde{\Delta}_g)Z]\}$  according to Eq. (14), respectively.  $E = 0.01\kappa$  is taken in (a) and (b). The other parameters are the same as given in Fig. 2.

$G_m$  is to destroy the PB effect rather than contribute to it. This is because when  $G_m = 0$ , there still are two transition pathways to access the two-photon state, i.e., (a)  $|00\rangle \xrightarrow{G} |20\rangle$  and (b)  $|00\rangle \xrightarrow{E} |10\rangle \xrightarrow{\sqrt{2}E} |20\rangle$ , which can ensure  $C_{20} = 0$ . The enhancement of  $G_m$  will actually weaken the interference effect, resulting in the increase of  $\log_{10}[g_a^{(2)}(0)]$ .

Besides for cavity-magnon coupling strength  $G_m$ , parametric gain  $G$  also has a positive effect on the generation of the MB. To confirm the dependence of  $\log_{10}[g_m^{(2)}(0)]$  on parametric gain  $G$ , we show, in Fig. 6(b),  $\log_{10}[g_m^{(2)}(0)]$  as a function of  $\Delta_c$  for various parametric gain  $G$ . For the parameters  $G$  and  $\theta$  given by Eq. (13), the function  $g_m^{(2)}(0)$  finds its minimum value as  $10^{-2.2}$  when  $\Delta_c/\kappa = 1$ . Nevertheless, the value of  $g_m^{(2)}(0)$  is one order of magnitude larger with  $G = 0.5G^{\text{opt}}$ . In particular, in the absence of parametric gain, no MB occurs for any driving detuning, which demonstrates that the parametric gain  $G$  has a significant contribution to the enhancement of the MB due to its involvement in the interference pathway of the two-magnon state.

In the discussion above, we have adopted  $\Delta_m = \Delta_c$  for simplicity. To verify whether  $\Delta_m = \Delta_c$  is the optimal relationship between two detunings for achieving strong MB, we plot  $\log_{10}[g_m^{(2)}(0)]$  as a function of  $\Delta_c/\kappa$  for different values of  $\Delta_m$ , namely,  $\Delta_m/\kappa = 0, 1, 2, 3$ , in Fig. 7(a). It is clearly observed that when  $\Delta_c/\kappa = 0, 1, 2, 3$ ,  $\log_{10}[g_m^{(2)}(0)]$  is smallest, respectively, corresponding to  $\Delta_m/\kappa = 0, 1, 2, 3$ , which confirms that  $\Delta_c = \Delta_m$  is the optimal relationship generating the strong MB. Furthermore,  $\log_{10}[g_m^{(2)}(0)]$  as a function of  $\Delta_c/\kappa$  is shown with  $\Delta_m = \Delta_c$  in Fig. 7(b), which reveals that the perfect MB occurs at different values of  $\Delta_c$  owing to the changes of optimal parameters  $G^{\text{opt}}$  and  $\theta^{\text{opt}}$ . It is worthwhile to note that when the optimal parameters are taken by absorbing  $\Delta_c/\kappa = \Delta_m/\kappa = 3$  into Eq. (13),  $\log_{10}[g_m^{(2)}(0)]$  takes local minimum values at  $\Delta_c/\kappa = \Delta_m/\kappa = \pm 3$ . This is because at  $\Delta_c/\kappa = \Delta_m/\kappa = \pm 3$ , there also exists  $G_m^2 = \Delta_c\Delta_m$ , which

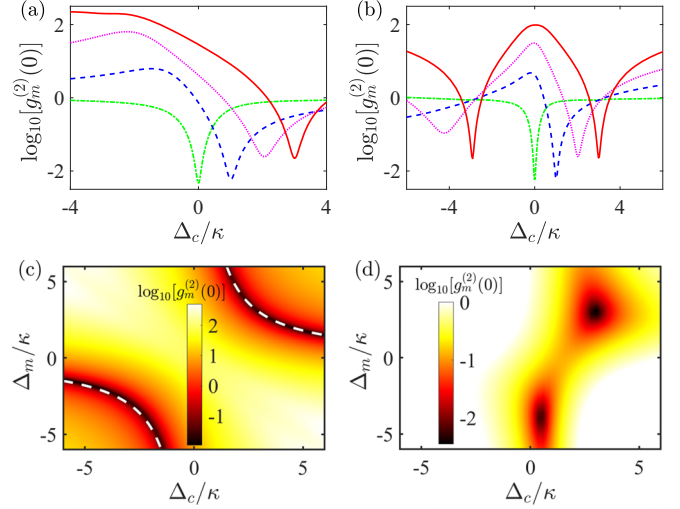


FIG. 7. (a) Second-order magnon correlation function on a logarithmic scale  $\log_{10}[g_m^{(2)}(0)]$  as a function of the driving detuning  $\Delta_c$  when  $\Delta_m/\kappa = 0, 1, 2, 3$  for different pairs of optimal parameters  $G$  and  $\theta$ . (b)  $\log_{10}[g_m^{(2)}(0)]$  as a function of  $\Delta_c = \Delta_m$  for different pairs of optimal parameters  $G$  and  $\theta$ , which result in the perfect MB occurring at  $\Delta_c/\kappa = 0, 1, 2, 3$ . In (a) and (b), different pairs of optimal parameters  $G$  and  $\theta$  are obtained by absorbing  $\Delta_c/\kappa = \Delta_m/\kappa = 0, 1, 2, 3$  into Eq. (13), respectively, corresponding to green, blue, pink, and red lines. (c), (d)  $\log_{10}[g_m^{(2)}(0)]$  as a function of  $\Delta_c$  and  $\Delta_m$ . The white dashed lines represent the optimal CMB condition  $G_m^2 = \Delta_c\Delta_m$ . The other parameters are the same as given in Fig. 2.

satisfies the condition for single-magnon excitation resonance. Therefore, for  $\Delta_c/\kappa = \Delta_m/\kappa = 3$ , the appearance of the MB combines the conditions of the CMB and the UMB, where  $\Delta_c/\kappa = \Delta_m/\kappa = 3$  along with other parameters can make sure optimal  $G$  and  $\theta$ . For  $\Delta_c/\kappa = \Delta_m/\kappa = -3$ , the MB is originated from the fulfillment of the single-magnon excitation resonance condition. To better understand this condition,  $\log_{10}[g_m^{(2)}(0)]$  as a function of  $\Delta_c/\kappa$  and  $\Delta_m/\kappa$  is presented in Fig. 7(c). The white dashed lines denote the CMB condition, i.e.,  $G_m^2 = \Delta_c\Delta_m$ . With the condition, the  $g_m^{(2)}(0)$  can be minimized, which indicates that the numerical results match the analytical solutions very well. In Fig. 7(d), with  $\kappa_m = 10\kappa_a$  and other parameters unchanged,  $g_m^{(2)}(0)$  is nearly one order of magnitude smaller. Meanwhile, the CMB condition is destroyed and the UMB condition is not affected by the ratio of two decay rates.

To further explain the important role of the parametric amplification in the generation of strong MB and illustrate the advantage of joint mechanisms for realizing the MB, we present the time-delay second-order correlation function  $\log_{10}[g_m^{(2)}(\tau)]$  for three cases in Fig. 8, that is, (i) without the parametric amplification ( $G = 0$ ); (ii) with  $G = G^{\text{opt}}$  and  $\Delta_c = 0$  (only satisfying the UMB condition); and (iii) with  $G = G^{\text{opt}}$  and  $\Delta_c = 3\kappa$  (satisfying simultaneous UMB and CMB conditions). As is predicted,  $g_m^{(2)}(\tau)$  is always equal to one when  $G$  is not considered. However, when  $G$  is taken as its optimal value, the strong MB can be realized. For  $\Delta_c = 0$ ,  $\log_{10}[g_m^{(2)}(\tau)]$  exhibits obvious oscillations, and  $\log_{10}[g_m^{(2)}(\tau)] > 0$  appears at certain moments, which corresponds to the UMB characteristic and indicates that high time

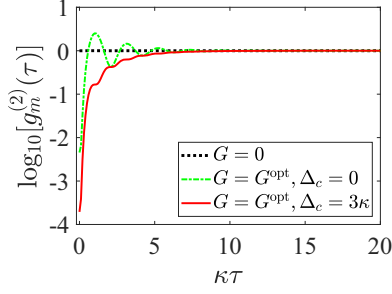


FIG. 8. Evolution of time-delay second-order correlation function  $\log_{10}[g_m^{(2)}(\tau)]$  vs time  $t$  for (i)  $G = 0$ , (ii)  $G = G^{\text{opt}}$ ,  $\Delta_c = 0$ , and (iii)  $G = G^{\text{opt}}$ ,  $\Delta_c/\kappa = 3$ . The other parameters are the same as given in Fig. 2.

resolution is required for observation. When  $G = G^{\text{opt}}$  and  $\Delta_c = 3\kappa$ ,  $\log_{10}[g_m^{(2)}(\tau)]$  gradually approaches zero, implying that high time resolution is not necessary and the joint detection of the single magnon becomes easier. Besides, the value of  $\log_{10}[g_m^{(2)}(0)]$  is less with  $\Delta_c = 3\kappa$  compared to  $\Delta_c = 0$  under a weaker driving strength  $E = 0.01\kappa$ . In other words, with  $G = G^{\text{opt}}$  and  $\Delta_c = 3\kappa$ , our scheme combines the advantages of the UMB and the CMB, that is, we can reduce  $g_m^{(2)}(0)$  and simultaneously avoid  $g_m^{(2)}(\tau)$  with oscillation during the evolution.

Finally, we investigate the thermal bath of the photon and the magnon on the MB. Introducing the thermal bath effect, the Lindblad operator  $\kappa\mathcal{L}[o]\rho$  in Eq. (5) should be rewritten as  $(\bar{n}_{th} + 1)\kappa\mathcal{L}[o]\rho + \bar{n}_{th}\kappa\mathcal{L}[o^\dagger]\rho$ , where the equilibrium thermal occupation numbers  $\bar{n}_{th} = \bar{n}_a, \bar{n}_m$ , respectively, correspond to  $o = a, m$ . As displayed in Figs. 9(a) and 9(b), the steady-state  $\log_{10}[g_m^{(2)}(0)]$  is plotted as a function of the thermal excitations  $\bar{n}_a$  and  $\bar{n}_m$  for different detunings, respectively. We find that  $\log_{10}[g_m^{(2)}(0)]$  increases as the thermal excitation numbers increase. The thermal excitations of the photon and magnon modes almost have the same influence on the MB. Moreover, for  $\Delta_c = 0$ , although  $\log_{10}[g_m^{(2)}(0)]$  is smallest at  $\bar{n}_a = 0$ , it is most susceptible to damage by the number of thermal excitations. In contrast, for  $\Delta_c = 3\kappa$ ,  $\log_{10}[g_m^{(2)}(0)]$  exhibits a greater robustness to the thermal excitations, approximately surviving up to  $\bar{n}_a, \bar{n}_m = 0.01$ . Comparing with other bosons, like phonons, the thermal occupations for the optical and magnetic systems are usually negligible. Therefore, the thermal bath for photon and magnon modes has an insignificant effect on the results.

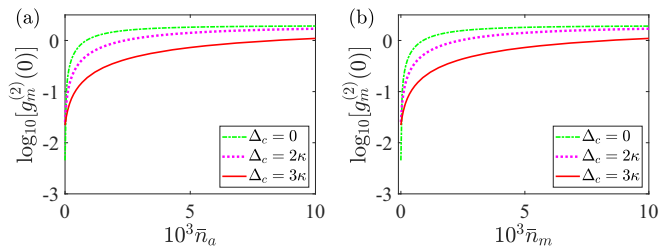


FIG. 9. Second-order magnon correlation function on a logarithmic scale  $\log_{10}[g_m^{(2)}(0)]$  as a function of (a) mean photon thermal occupation  $\bar{n}_a$  and (b) mean magnon thermal occupation  $\bar{n}_m$  for different frequency detuning  $\Delta_c/\kappa = (0, 2, 3)$  under the optimal UMB condition. The other parameters are the same as given in Fig. 2.

In view of the rapid advancement of experimental technology, our proposal holds the potential to be implemented in various physical systems, including whispering-gallery-mode (WGM) microcavities [66–68]. In optical WGM systems, introducing an OPA into the high-quality cavity can be achieved through the cavity boosted second-order or third-order optical nonlinearity [69,70]. In particular, the second-order nonlinearity in the WGM cavity can be utilized as the OPA to construct an optomechanical system [69]. On the other hand, it has been experimentally confirmed that the strong or ultrastrong coupling between YIG magnons and cavity photons can be realized by a magnetic dipole interaction [5–8]. Therefore, our hybrid system consisting of an OPA introduced to a optomechanical-magnonic system holds the promise to be feasible in experiment.

#### IV. CONCLUSIONS

In conclusion, we have proposed a scheme to generate and enhance the MB in a hybrid optomechanical-magnetic system with an OPA through quantum destructive interference between different transition pathways. Under the condition of weak optomechanical coupling, we can eliminate the mechanical mode and thus the system is reduced to a two-mode system, including magnon and photon modes. We analytically obtain optimal parameters  $G$  and  $\theta$ , which is shown to be in excellent agreement with the numerical results. With these optimal parameters, we observe that the second-order magnon correlation function decreases as the cavity-magnon coupling strength increases. Indeed, the dipole magnetic interaction plays a crucial role in the realization of the MB since it participates in every transition pathway to access the two-magnon state. Moreover, we demonstrate that by utilizing different optimal parameters  $G$  and  $\theta$ , we can flexibly adjust the driving detunings of the magnon and photon modes to achieve the minimum second-order magnon correlation function. Interestingly, with a specific driving detuning and optimal parameters  $G$  and  $\theta$ , we can harness the advantages of destructive interference and energy-level anharmonicity, which guarantees the reduction of equal-time second-order magnon correlation and eliminates rapid oscillations of the time-delay second-order magnon correlation. Furthermore, we find that our blockade scheme under optimized conditions is robust against the thermal noises. Our work paves a way towards magnon manipulation at the few-magnon state and may have potential applications in producing single-magnon emitters [71,72], which refers to a system or structure that can locally excite and produce a single magnon. The generation and propagation of magnons are inevitably closely related to their medium, but our work focuses on how to effectively control the local generation of a few-magnon state.

#### ACKNOWLEDGMENTS

This work was supported by the Natural Science Foundation of Jilin Province under Grant No. 20240101013JC and the National Natural Science Foundation of China under Grants No. 12375020, No. 12074330, No. 62071412, and No. 12074094.

- [1] V. Scarani, H. Bechmann-Pasquinucci, N. J. Cerf, M. Dušek, N. Lütkenhaus, and M. Peev, The security of practical quantum key distribution, *Rev. Mod. Phys.* **81**, 1301 (2009).
- [2] V. Giovannetti, S. Lloyd, and L. Maccone, Advances in quantum metrology, *Nat. Photon.* **5**, 222 (2011).
- [3] E. Knill, R. Laflamme, and G. J. Milburn, A scheme for efficient quantum computation with linear optics, *Nature (London)* **409**, 46 (2001).
- [4] P. Kok, W. J. Munro, K. Nemoto, T. C. Ralph, J. P. Dowling, and G. J. Milburn, Linear optical quantum computing with photonic qubits, *Rev. Mod. Phys.* **79**, 135 (2007).
- [5] Y. Tabuchi, S. Ishino, T. Ishikawa, R. Yamazaki, K. Usami, and Y. Nakamura, Hybridizing ferromagnetic magnons and microwave photons in the quantum limit, *Phys. Rev. Lett.* **113**, 083603 (2014).
- [6] J. Bourhill, N. Kostylev, M. Goryachev, D. L. Creedon, and M. E. Tobar, Ultrahigh cooperativity interactions between magnons and resonant photons in a YIG sphere, *Phys. Rev. B* **93**, 144420 (2016).
- [7] M. Goryachev, W. G. Farr, D. L. Creedon, Y. Fan, M. Kostylev, and M. E. Tobar, High-cooperativity cavity QED with magnons at microwave frequencies, *Phys. Rev. Appl.* **2**, 054002 (2014).
- [8] D. Zhang, X. M. Wang, T. F. Li, X. Q. Luo, W. Wu, F. Nori, and J. Q. You, Cavity quantum electrodynamics with ferromagnetic magnons in a small yttrium-iron-garnet sphere, *npj Quantum Inf.* **1**, 15014 (2015).
- [9] X. Zhang, C. L. Zou, L. Jiang, and H. X. Tang, Cavity magnomechanics, *Sci. Adv.* **2**, e1501286 (2016).
- [10] D. Lachance-Quirion, Y. Tabuchi, A. Gloppe, K. Usami, and Y. Nakamura, Hybrid quantum systems based on magnonics, *Appl. Phys. Express* **12**, 070101 (2019).
- [11] Z. X. Yang, L. Wang, Y. M. Liu, D. Y. Wang, C. H. Bai, S. Zhang, and H. F. Wang, Ground state cooling of magnomechanical resonator in  $\mathcal{PT}$ -symmetric cavity magnomechanical system at room temperature, *Front. Phys.* **15**, 52504 (2020).
- [12] Q. Liao, Y. Zeng, M. Song, and H. Qiu, Ground-state cooling of magnomechanical resonator in a cavity magnomechanical system with double-passage, *Europhys. J. Plus* **138**, 868 (2023).
- [13] M. Asjad, J. Li, S. Y. Zhu, and J. Q. You, Magnon squeezing enhanced ground-state cooling in cavity magnomechanics, *Fundament. Res.* **3**, 3 (2023).
- [14] J. Li, S. Y. Zhu, and G. S. Agarwal, Magnon-photon-phonon entanglement in cavity magnomechanics, *Phys. Rev. Lett.* **121**, 203601 (2018).
- [15] Z. Y. Fan, H. Qian, X. Zuo, and J. Li, Entangling ferrimagnetic magnons with an atomic ensemble via optomagnomechanics, *Phys. Rev. A* **108**, 023501 (2023).
- [16] W. Zhang, D. Y. Wang, C. H. Bai, T. Wang, S. Zhang, and H. F. Wang, Generation and transfer of squeezed states in a cavity magnomechanical system by two-tone microwave fields, *Opt. Express* **29**, 11773 (2021).
- [17] J. Li, S. Y. Zhu, and G. S. Agarwal, Squeezed states of magnons and phonons in cavity magnomechanics, *Phys. Rev. A* **99**, 021801(R) (2019).
- [18] Z. X. Liu, H. Xiong, and Y. Wu, Magnon blockade in a hybrid ferromagnet-superconductor quantum system, *Phys. Rev. B* **100**, 134421 (2019).
- [19] L. Wang, Z. X. Yang, Y. M. Liu, C. H. Bai, D. Y. Wang, S. Zhang, and H. F. Wang, Magnon blockade in a  $\mathcal{PT}$ -symmetric-like cavity magnomechanical system, *Ann. Phys.* **532**, 2000028 (2020).
- [20] J. K. Xie, S. L. Ma, and F. L. Li, Quantum-interference-enhanced magnon blockade in an yttrium-iron-garnet sphere coupled to superconducting circuits, *Phys. Rev. A* **101**, 042331 (2020).
- [21] F. Wang, C. Gou, J. Xu, and C. Gong, Hybrid magnon-atom entanglement and magnon blockade via quantum interference, *Phys. Rev. A* **106**, 013705 (2022).
- [22] C. Zhao, X. Li, S. Chao, R. Peng, C. Li, and L. Zhou, Simultaneous blockade of a photon, phonon, and magnon induced by a two-level atom, *Phys. Rev. A* **101**, 063838 (2020).
- [23] Y. J. Xu, T. le Yang, L. Lin, and J. Song, Conventional and unconventional magnon blockades in a qubit-magnon hybrid quantum system, *J. Opt. Soc. Am. B* **38**, 876 (2021).
- [24] A. Imamoğlu, H. Schmidt, G. Woods, and M. Deutsch, Strongly interacting photons in a nonlinear cavity, *Phys. Rev. Lett.* **79**, 1467 (1997).
- [25] S. Ghosh and T. C. H. Liew, Dynamical blockade in a single-mode bosonic system, *Phys. Rev. Lett.* **123**, 013602 (2019).
- [26] F. Zou, D. G. Lai, and J. Q. Liao, Enhancement of photon blockade effect via quantum interference, *Opt. Express* **28**, 16175 (2020).
- [27] D. Y. Wang, C. H. Bai, Y. Xing, S. Liu, S. Zhang, and H. F. Wang, Enhanced photon blockade via driving a trapped  $\Lambda$ -type atom in a hybrid optomechanical system, *Phys. Rev. A* **102**, 043705 (2020).
- [28] K. M. Birnbaum, A. Boca, R. Miller, A. D. Boozer, T. E. Northup, and H. J. Kimble, Photon blockade in an optical cavity with one trapped atom, *Nature (London)* **436**, 87 (2005).
- [29] C. J. Zhu, Y. P. Yang, and G. S. Agarwal, Collective multiphoton blockade in cavity quantum electrodynamics, *Phys. Rev. A* **95**, 063842 (2017).
- [30] T. Peyronel, O. Firstenberg, Q. Y. Liang, S. Hofferberth, A. V. Gorshkov, T. Pohl, M. D. Lukin, and V. Vuletić, Quantum nonlinear optics with single photons enabled by strongly interacting atoms, *Nature (London)* **488**, 57 (2012).
- [31] D. Y. Wang, C. H. Bai, X. Han, S. Liu, S. Zhang, and H. F. Wang, Enhanced photon blockade in an optomechanical system with parametric amplification, *Opt. Lett.* **45**, 2604 (2020).
- [32] M. Bamba, A. Imamoğlu, I. Carusotto, and C. Ciuti, Origin of strong photon antibunching in weakly nonlinear photonic molecules, *Phys. Rev. A* **83**, 021802(R) (2011).
- [33] X. W. Xu and Y. Li, Tunable photon statistics in weakly nonlinear photonic molecules, *Phys. Rev. A* **90**, 043822 (2014).
- [34] D. Gerace and V. Savona, Unconventional photon blockade in doubly resonant microcavities with second-order nonlinearity, *Phys. Rev. A* **89**, 031803(R) (2014).
- [35] Y. H. Zhou, H. Z. Shen, and X. X. Yi, Unconventional photon blockade with second-order nonlinearity, *Phys. Rev. A* **92**, 023838 (2015).
- [36] J. Tang, W. Geng, and X. Xu, Quantum interference induced photon blockade in a coupled single quantum dot-cavity system, *Sci. Rep.* **5**, 9252 (2015).
- [37] H. Flayac and V. Savona, Unconventional photon blockade, *Phys. Rev. A* **96**, 053810 (2017).



- [38] E. Zubizarreta Casalengua, J. C. López Carreño, F. P. Laussy, and E. D. Valle, Conventional and unconventional photon statistics, *Laser Photon. Rev.* **14**, 1900279 (2020).
- [39] M. S. Kheirabady, E. Ghasemian, and M. K. Tavassoly, Magnon blockade and magnon–atom entanglement induced by a qutrit coupled to a ferromagnetic YIG sphere, *Ann. Phys.* **535**, 2300024 (2023).
- [40] X. Li, X. Wang, Z. Wu, W. X. Yang, and A. X. Chen, Tunable magnon antibunching in a hybrid ferromagnet-superconductor system with two qubits, *Phys. Rev. B* **104**, 224434 (2021).
- [41] K. Wu, W. X. Zhong, G. L. Cheng, and A. X. Chen, Phase-controlled multimagnon blockade and magnon-induced tunneling in a hybrid superconducting system, *Phys. Rev. A* **103**, 052411 (2021).
- [42] M. S. Ebrahimi and M. B. Harouni, Parity-time symmetry-enhanced simultaneous magnon and photon blockade in cavity magnonic system, *J. Phys. B: At. Mol. Opt. Phys.* **56**, 235501 (2023).
- [43] C. P. Shen, J. Q. Chen, X. F. Pan, Y. M. Ren, X. L. Dong, X. L. Hei, Y. F. Qiao, and P. B. Li, Tunable nonreciprocal photon correlations induced by directional quantum squeezing, *Phys. Rev. A* **108**, 023716 (2023).
- [44] D. W. Liu, K. W. Huang, Y. Wu, and L. G. Si, Parametric amplification induced giant nonreciprocal unconventional photon blockade in a single microring resonator, *Appl. Phys. Lett.* **123**, 061103 (2023).
- [45] R. Huang, A. Miranowicz, J.-Q. Liao, F. Nori, and H. Jing, Nonreciprocal photon blockade, *Phys. Rev. Lett.* **121**, 153601 (2018).
- [46] B. Li, R. Huang, X. Xu, A. Miranowicz, and H. Jing, Nonreciprocal unconventional photon blockade in a spinning optomechanical system, *Photon. Res.* **7**, 630 (2019).
- [47] W. Zhang, T. Wang, S. Liu, S. Zhang, and H. F. Wang, Nonreciprocal photon blockade in a spinning resonator coupled to two two-level atoms, *Sci. China Phys. Mech. Astron.* **66**, 240313 (2023).
- [48] L. A. Wu, H. J. Kimble, J. L. Hall, and H. Wu, Generation of squeezed states by parametric down conversion, *Phys. Rev. Lett.* **57**, 2520 (1986).
- [49] X. Y. Lü, Y. Wu, J. R. Johansson, H. Jing, J. Zhang, and F. Nori, Squeezed optomechanics with phase-matched amplification and dissipation, *Phys. Rev. Lett.* **114**, 093602 (2015).
- [50] W. Qin, A. Miranowicz, P. B. Li, X. Y. Lü, J. Q. You, and F. Nori, Exponentially enhanced light-matter interaction, cooperativities, and steady-state entanglement using parametric amplification, *Phys. Rev. Lett.* **120**, 093601 (2018).
- [51] Y. Wang, J. L. Wu, J. X. Han, Y. Xia, Y. Y. Jiang, and J. Song, Enhanced phonon blockade in a weakly coupled hybrid system via mechanical parametric amplification, *Phys. Rev. Appl.* **17**, 024009 (2022).
- [52] X. Guo, C. L. Zou, H. Jung, and H. X. Tang, On-chip strong coupling and efficient frequency conversion between telecom and visible optical modes, *Phys. Rev. Lett.* **117**, 123902 (2016).
- [53] J. Q. Wang, Y. H. Yang, M. Li, X. X. Hu, J. B. Surya, X. B. Xu, C. H. Dong, G. C. Guo, H. X. Tang, and C. L. Zou, Efficient frequency conversion in a degenerate  $\chi^{(2)}$  microresonator, *Phys. Rev. Lett.* **126**, 133601 (2021).
- [54] Z. Ma, J. Y. Chen, Z. Li, C. Tang, Y. M. Sua, H. Fan, and Y. P. Huang, Ultrabright quantum photon sources on chip, *Phys. Rev. Lett.* **125**, 263602 (2020).
- [55] L. Tang, J. Tang, M. Chen, F. Nori, M. Xiao, and K. Xia, Quantum squeezing induced optical nonreciprocity, *Phys. Rev. Lett.* **128**, 083604 (2022).
- [56] Y. Wei, B. Xiong, C. Shan, J. Liu, and X. Wang, Phonon blockade in a quadratically coupled optomechanical system with two-phonon driving, *Results Phys.* **44**, 106202 (2023).
- [57] C. H. Bai, D. Y. Wang, S. Zhang, and H. F. Wang, Qubit-assisted squeezing of mirror motion in a dissipative cavity optomechanical system, *Sci. China Phys. Mech. Astron.* **62**, 970311 (2019).
- [58] C. H. Bai, D. Y. Wang, S. Zhang, S. Liu, and H. F. Wang, Modulation-based atom-mirror entanglement and mechanical squeezing in an unresolved-sideband optomechanical system, *Ann. Phys.* **531**, 1800271 (2019).
- [59] S. Huang and G. S. Agarwal, Enhancement of cavity cooling of a micromechanical mirror using parametric interactions, *Phys. Rev. A* **79**, 013821 (2009).
- [60] J. H. Gan, Y. C. Liu, C. Lu, X. Wang, M. K. Tey, and L. You, Intracavity-squeezed optomechanical cooling, *Laser Photon. Rev.* **13**, 1900120 (2019).
- [61] V. Peano, H. G. L. Schwefel, C. Marquardt, and F. Marquardt, Intracavity squeezing can enhance quantum-limited optomechanical position detection through deamplification, *Phys. Rev. Lett.* **115**, 243603 (2015).
- [62] X. Fu, X. Guo, and S. Chester, Raman-enhanced phase-sensitive fibre optical parametric amplifier, *Sci. Rep.* **6**, 20180 (2016).
- [63] Y. Y. Jiang, A. D. Ludlow, N. D. Lemke, R. W. Fox, J. A. Sherman, L. S. Ma, and C. W. Oates, Making optical atomic clocks more stable with  $10^{-16}$ -level laser stabilization, *Nat. Photon.* **5**, 158 (2011).
- [64] T. M. Fortier, M. S. Kirchner, F. Quinlan, J. Taylor, J. C. Bergquist, T. Rosenband, N. Lemke, A. Ludlow, Y. Jiang, C. W. Oates, and S. A. Diddams, Generation of ultrastable microwaves via optical frequency division, *Nat. Photon.* **5**, 425 (2011).
- [65] J. R. Johansson, P. D. Nation, and F. Nori, QuTiP: An open-source Python framework for the dynamics of open quantum systems, *Comput. Phys. Commun.* **183**, 1760 (2012).
- [66] M. Aspelmeyer, T. J. Kippenberg, and F. Marquardt, Cavity optomechanics, *Rev. Mod. Phys.* **86**, 1391 (2014).
- [67] Z. Shen, Y. L. Zhang, Y. Chen, C. L. Zou, Y. F. Xiao, X. B. Zou, F. W. Sun, G. C. Guo, and C. H. Dong, Experimental realization of optomechanically induced non-reciprocity, *Nat. Photon.* **10**, 657 (2016).
- [68] V. S. Ilchenko, A. A. Savchenkov, A. B. Matsko, and L. Maleki, Nonlinear optics and crystalline whispering gallery mode cavities, *Phys. Rev. Lett.* **92**, 043903 (2004).
- [69] M. Förtsch, J. U. Fürst, C. Wittmann, D. Strekalov, A. Aiello, M. V. Chekhova, C. Silberhorn, G. Leuchs, and C. Marquardt, A versatile source of single photons for quantum information processing, *Nat. Commun.* **4**, 1818 (2013).
- [70] T. J. Kippenberg, S. M. Spillane, and K. J. Vahala, Kerr-nonlinear optical parametric oscillation in an ultrahigh-Q toroid microcavity, *Phys. Rev. Lett.* **93**, 083904 (2004).

- [71] D. Ghazaryan, M. T. Greenaway, Z. Wang, V. H. Guarochico Moreira, I. J. Vera-Marun, J. Yin, Y. Liao, S. V. Morozov, O. Kristanovski, A. I. Lichtenstein, M. I. Katsnelson, F. Withers, A. Mishchenko, L. Eaves, A. K. Geim, K. S. Novoselov, and A. Misra, Magnon-assisted tunnelling in van der Waals heterostructures based on CrBr<sub>3</sub>, *Nat. Electron.* **1**, 344 (2018).
- [72] M. Evelt, L. Soumah, A. B. Rinkevich, S. O. Demokritov, A. Anane, V. Cros, J. BenYoussef, G. deLoubens, O. Klein, P. Bortolotti, and V. E. Demidov, Emission of coherent propagating magnons by insulator-based spin-orbit-torque oscillators, *Phys. Rev. Appl.* **10**, 041002(R) (2018).